Eddy iron fluxes control primary production in the Southern Ocean

Leading author: Takaya Uchida (takaya@ldeo.columbia.edu)

Eddy iron fluxes control primary production in the open Southern Ocean

Takaya Uchida[1], Dhruv Balwada[3], Ryan Abernathey[1,2], Galen McKinley[1,2], Shafer Smith[3] & Marina Lévy[4]

[1]*Department of Earth and Environmental Sciences, Columbia University in the City of New York*

[2]*Division of Ocean and Climate Physics, Lamont-Doherty Earth Observatory*

[3]*Center for Atmosphere Ocean Science, Courant Institute of Mathematical Sciences, New York University*

[4]*Laboratoire d'Océanographie et du Climat, Institut Pierre Simon-Laplace*

Primary productivity of the Southern Ocean ecosystem, and the associated biological carbon pump, is limited by the availability of the micronutrient iron. Riverine sediments and atmospheric dust supply iron at the ocean margins, but in the vast open ocean iron reaches phytoplankton primarily when iron-rich sub-surface waters enter the euphotic zone, linking vertical transport processes to ecosystem productivity. Existing estimates of vertical iron transport focus on one-dimensional processes such as mixed-layer entrainment; however, evidence from the North Atlantic and from Lagrangian simulations suggests that eddy transport may be a highly effective pathway for nutrient supply. In this study, high-resolution physical/biogeochemical simulations of an open-Southern-Ocean ecosystem forced with a realistic seasonal cycle reveal that iron transport across the mixed layer base is primarily due to (sub)mesoscale eddies. As model resolution is increased from 20 km to 5 km to 2 km,

vertical eddy iron flux and phytoplankton biomass increase strongly, despite shoaling of the mixed layer. Diagnostics from eddy resolving and parametrized runs show that this transport is predominantly associated with (sub)mesoscale isopycnal stirring, rather than mixed-layer instability. One important consequence is that iron recycling is second-order importance in explaining sustained summertime productivity, as eddies continue to supply iron to the mixed layer throughout the year. Since eddy mixing rates are sensitive to wind forcing and large-scale hydrographic changes, these findings open a new mechanism for modulating the Southern Ocean biogeochemical pump on climate timescales.

Budgets of iron, the limiting nutrient in the Southern Ocean for primary production (1; 2; 3), from ship-track observations have emphasized the importance of dust deposition, lateral transport and remineralization of iron, concluding that contributions from upwelling is negligible (4). More recently, however, one-dimensional process studies have highlighted the importance of mixed-layer entrainment (5) and vertical diffusion of iron (6) in regions remote from dust sources. Due to the sparse spatial and temporal coverage of in-situ iron observations and the intermittent nature of iron supply and phytoplankton blooms, a basin-scale view has generally relied on global circulation models (GCMs; 7; 8) and data assimilation products (9). A GCM intercomparison study showed that, although the iron sources and biogeochemical parameters varied widely, the global-mean iron concentrations were largely in agreement, a consequence of model tuning towards this target (10). When compared against individual ocean transects, however, the GCMs showed a large inter-model disagreement. This spread was attributed to differences in how each model represented the scavenging of iron. Due to computational constraints, eddy iron transport in GCMs must be

parametrized, also potentially causing uncertainty in the physical processes transporting iron (11).

In addition to vertical diapycnal mixing and large-scale circulation, mesoscale eddies (on scales of roughly 20 - 200 km) can make a major contribution to tracer transport (12; 13). In the Southern Ocean, upward vertical mesoscale eddy heat fluxes counteract the downward flux of heat due to Ekman pumping (14), and mesoscale eddies help regulate the subduction of anthropogenic carbon from the surface into the interior (11; 15). At even smaller scales where the geostrophic approximation breaks down, submesoscale turbulence (roughly 1 - 20 km) generates vigorous vertical velocities near the surface (16). In the North Atlantic, submesoscale turbulence has been argued to drive significant transport of nutrients across the mixed-layer base, supporting ecosystem productivity (17). Do eddies play the same role with iron in the Southern Ocean?

To our knowledge, this question has only been investigated by examining Lagrangian particle trajectories from a high-resolution numerical simulation of the Kerguelen region. Calculating iron concentration in the reference frame of Lagrangian particles, Rosso (18; 19) argued that submesoscale iron fluxes could enhance primary productivity by a factor of two. While suggestive, their simulation technique did not implement a full ecosystem model, account for the strong seasonal cycle in both turbulence and biology, nor include fluxes from vertical mixing or mixed-layer entrainment. The relative contribution of eddies to the open-Southern-Ocean iron budget therefore warrants further investigation.

Here we take a different approach: we run a very high resolution numerical simulation in an idealized channel configuration and force the model with a realistic seasonal cycle. Due to the ap-

proximate zonal symmetry of the Antarctic Circumpolar Current, such configurations can capture the broad characteristics of Southern Ocean circulation, tracer transport and ventilation (20; 21). The reduced computational cost (compared to a global-scale simulation) enables our model to reach physical and biogeochemical equilibrium, and the simple geometry facilitates straightforward interpretation of the dynamics. Varying the spatial resolution of the model allows us to explore the impacts of explicitly resolved — as opposed to parameterized — eddy iron fluxes on primary production.

Submesoscale permitting simulation of the open Southern Ocean ecosystem

We use the Masachusetts Institute of Technology general circulation model (22) (MITgcm) with an embedded full ecosystem model (23; 24). Details of the model set up are given in Text S1 (Supplementary Information). A snapshot of the phytoplankton biomass and iron field in the top 300 m on November 1 from the 2 km run, during the height of spring bloom, is shown in Fig. 1. The Rossby deformation radius at the center of the domain is 14 km, so the horizontal resolution of 2 km allows us to observe the imprint of mesoscale coherent features (25), such as fronts and eddies, in both iron and phytoplankton.

To simulate the interaction of this region with the rest of the ocean, iron and other nutrients are relaxed to climatological observational profiles at the Northern boundary; in the rest of the domain their concentrations evolve freely based on the simulated circulation and ecosystem. In order to isolate the role of open-ocean transport processes, we do not supply aeolian dust input

at the surface or glacial and bathymetric iron sources from the south. The annual-zonal-mean iron transect (Fig. 1**c**) shows enhanced iron concentrations at depth and strong depletion near the surface. A comparison with Geotraces iron profiles from the Southern Ocean (Fig. 1**d**) indicates that our simulation has a realistic ferrocline structure, in contrast with most of the global-scale GCM simulations (10). Deep iron concentrations of roughly 0.4 μmol Fe m^{-3} at 1000 m coincide with the observational mean in the ACC, while near-surface concentrations (0.05 μmol Fe m^{-3}) are lower than the observational range. This discrepancy is likely due to the lack of aeolian, glacial and bathymetric sources (26), uncertainty in the ecosystem model parameters (10), and potentially due to the lack of storms which have been argued to enhance diffusive entrainment of iron from the interior (Nicholson, S., Lévy, M., Jouanno, J., Capet, X., Swart, S. & Monteiro, P., submitted to *Geophys. Res. Let.*; hereon Nicholson, S. *et al*., submitted). As a result, iron is the limiting nutrient year round in our simulations, while in the real ACC, silicate limitation is also expected to control diatom growth and transition in phytoplankton community composition (7; 8). Consequently, primary production in our model is biased slightly low, particularly over the summer (Text S2, Figs. S1, S2).

The Southern Ocean ecosystem is highly seasonal, with a strong spring bloom occurring between November and January (28; 29). Figure 2 illustrates the simulated climatological seasonal cycle of important physical and biological quantities, averaged over the center of the domain. As our simulations are able to reproduce this seasonal cycle, they provide a unique opportunity to investigate how seasonality in biological processes interacts with the seasonal cycle in physical transport processes and mixing-layer depth (MLD; definition in Methods section). There is a

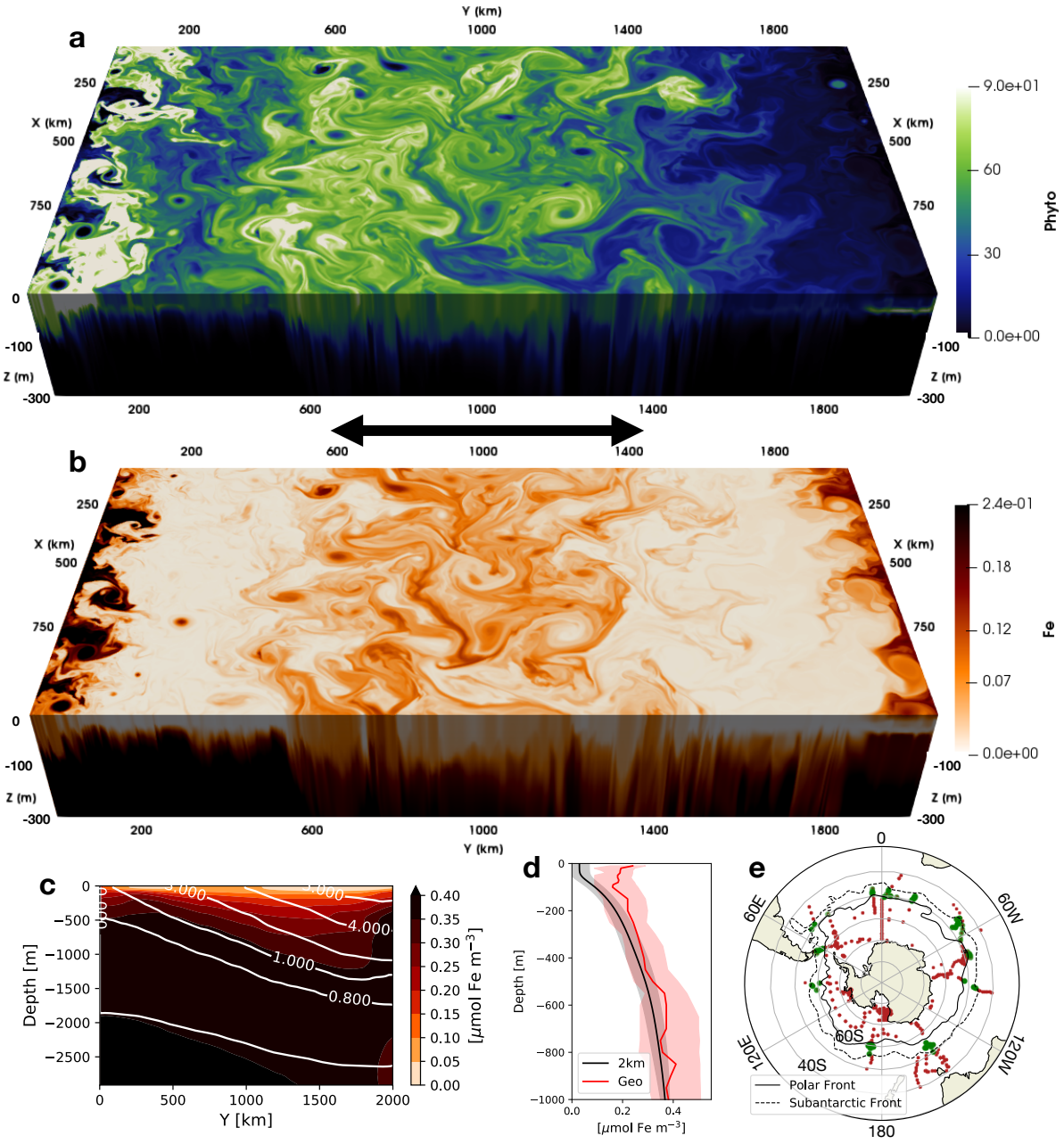

Figure 1: **A snapshot of phytoplankton biomass in (mg C m^{-3}) and iron in (μmol Fe m^{-3}) in the top 300 m; a,b. c** The zonal mean transect of iron and **d** vertical profile averaged over the meridional extent of y = 600 - 1400 km shown as the black arrow in **a** for our 2 km run (black) and median of the Geotraces dataset (red) acquired through personal communication with Tagliabue (6) over all profiles in the open ocean region between the climatological position of Polar and Subantarctic front (green; **e**) after applying a three-point median filter in the vertical. The frontal positions were taken from (27) and extended by 1° to the south and north respectively to incorporate more profiles. The colored shading show the standard deviation for the 2 km run and due to the lack of spatial coverage, the interquartile range is shown for Geotraces. The Geotraces dataset was biased towards austral summer so the data used in **d** for the 2 km run is over Nov.-Feb.

strong spring bloom, with the vertically integrated phytoplankton biomass ($\langle C_p \rangle$; definition given in Methods section) peaking in early November, after the wintertime MLD has started to shoal (Fig. 2**a**), consistent with previous characterizations of the spring bloom in the ACC (29). To characterize the strength of (sub)mesoscale turbulence, we also show the root-mean square of vertical velocity ($\overline{w^2}^{1/2}$), which mirrors the MLD closely. This suggests that the vertical velocities are associated with mixed-layer instability (MLI), a type of surface-intensified baroclinic instability driven by available potential energy within the mixed layer and is associated with submesoscales (30), which is more active in winter with deep mixed layers.

The spring bloom is quantified via $\langle C_p \rangle$, which allows us to define the bloom *onset* ($\langle C_p \rangle$ minimum) and *apex* ($\langle C_p \rangle$ maximum) (Fig. 2**a**; (31)). The onset is in late July during the deepening of wintertime mixing layer, and the apex occurs in early November even though surface light conditions (γ^I; eqn. (S3)) continue to improve over the summer (November-January; Fig. 2**b**). The decrease in nutrient limitation factor (γ^N; eqn. (S4)), on the other hand, from 0.8 to 0.2 coincides with the apex and is in phase with iron concentration dropping from 0.13 to 0.03 μmol m^{-3} (Fig. 2**b**). (The limitation factors ("γ"s $= 0$ - 1) indicate ideal growth conditions when they are unity and zero for no-growth conditions. The effect of grazing by zooplankton is shown in Text S3, Fig. S3.) This indicates that the decline of the spring bloom in our simulation is due to iron limitation, and not associated with light conditions.

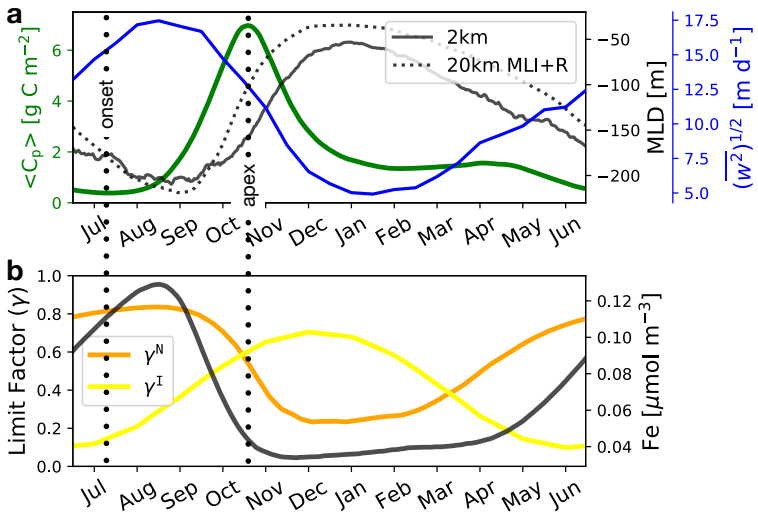

Figure 2: **Time series of the daily-mean vertically integrated phytoplankton biomass ($\langle \mathbf{C_p} \rangle$; green), daily mean of MLD for the 2 km (black solid) and 20 km MLI+R run (black dotted) averaged over the meridional extent of $y = 600$ - 1400 km; a.** The seasonal cycle of the root mean square of vertical velocity averaged over the same meridional extent and over 100 m depth from the 2 km run ($\overline{w^2}^{1/2}$) is shown in blue. **b.** The spatial median over the top 100 m of growth rate limitation factors due to nutrient (γ^{N}; orange) and light (γ^{I}; yellow) where the former is due to iron year round in our simulation. The iron concentration averaged over the top 100 m in black is plotted against the right axis.

Vertical eddy and diffusive iron transport

To understand what controls the iron concentrations, we now examine the ecosystem in the time-depth plane. The top row of Fig. 3 shows horizontally averaged phytoplankton concentration and vertical iron fluxes by eddies and diffusion vs. time and depth over the climatological seasonal cycle from the 2 km run. Iron concentration is given in Fig. 3**f** showing signals of wintertime entrainment with the orange contours dipping into the ML around September. (We show the complete zonal-mean iron budget in Fig. S1 and time-depth plots of biogeochemical iron consumption in Fig. S2.) As in Fig. 2**a**, there is a strong spring bloom and a mild autumn bloom. Some phytoplankton live below the ML base, particularly during summer when the ML is shallow. During wintertime (July-September) when the ML is deepening and light is low, there is low biomass but

high iron concentration (Fig. 3**a**,**f**), consistent with light limitation factor ($\gamma^{I,N}$, Fig. 2**b**).

Iron is supplied to the phytoplankton via three processes: remineralization, entrainment and vertical mixing (here associated with the K-profile parametrization boundary layer; KPP (32)), and vertical eddy fluxes (explicitly resolved by the simulation). Figures 3**b**,**c** and S1 show how eddies and vertical mixing work together to deliver iron to phytoplankton from depth. Vertical mixing is, by construction, only active within the ML. When vertical gradients of iron are actively sustained by biological consumption (e.g. during the bloom), vertical mixing drives a strong upward diffusive iron flux. This diffusive flux goes to zero at the ML base where KPP turns off. Eddy fluxes, in contrast, peak roughly at the ML base and extend deep into the iron-rich interior, with a magnitude comparable to the diffusive flux in the ML. Thus, eddies play a crucial role in bringing iron across the ML base, where it can be handed off to vertical mixing and delivered to near-surface phytoplankton.

Vertical eddy iron transport is absent from previous estimates of the Southern Ocean iron budget (4; 5; 6). One-dimensional iron budgets suggest that during summer, vertical mixing is not strong enough to supply the iron needed to sustain the observed productivity, implying strong iron recycling within the ecosystem (6). Our simulations challenge this conclusion, showing that vertical eddy transport can provide a year-round source of iron (Fig. 3**b**) which exceeds the magnitude of iron remineralization (Fig. S1).

With the 2 km run as a reference, we use spatial resolution as a parameter to modulate the strength of eddy transport, running two other simulations at eddy-permitting resolutions of 5 km

and 20 km. The basin-wide density and iron stratification for each resolution are given in Fig. S4. Figure 4 shows the annual median of vertically integrated phytoplankton biomass plotted against the annual mean of total (dominated by eddy) vertical iron flux across the ML base, or 100 m, whichever is deeper. This depth scale is chosen to exclude KPP mixing from the flux, and is roughly the depth phytoplankton cease to exist (Fig. 3**a**,**c**). As resolution increases from 20 km to 2 km for runs without any eddy parametrizations (red markers in Fig. 4), the annual median of daily averaged phytoplankton biomass ($\overline{\langle \mathrm{C_p} \rangle}$) nearly doubles from 0.67 to 1.45 g C m^{-2} in a roughly linear relationship with the annual-mean total (eddy+diffusive) iron transport (F^z_{Fe}), which increases from 7 to 27 μmol Fe m^{-2} yr^{-1}. This occurs despite a shoaling of the ML, which reduces the entrainment of iron. Thus, in our model ecosystem, eddies effectively control the ecosystem primary productivity.

[Sub]mesoscale eddy parametrizations

As we move to lower resolution, we also ask whether conventional eddy parameterizations can provide the missing iron flux. We run three additional simulations at 100 km and 20 km resolution. The former represents a standard Coupled Model Intercomparison Project (CMIP)-class ocean GCM, while the latter the newer class of mesoscale-permitting GCMs (33). We experiment with three different eddy parameterizations: Gent-McWilliams' eddy-induced velocity parametrization (GM; 34; 35), isopycnal tracer diffusion (Redi; 36), and mixed-layer instability (MLI) parametrization (37), each representing different physical mechanisms. The runs are:

- `100 km GM+R` – with GM and Redi, to represent unresolved mesoscale restratification in addition to stirring in the interior at 100 km resolution. We allowed the GM coefficient to vary between 200-2500 $m^2\ s^{-1}$, depending on the vertical-mean Richardson number (38), and chose a tapering scheme which accounted for a smooth transition between the diabatic boundary layer and adiabatic interior (39). The Redi diffusivity was chosen as 1000 $m^2\ s^{-1}$.

- `20 km MLI+R` – with MLI and Redi, to represent the shoaling of the ML due to otherwise resolved MLI and unresolved mesoscale iron stirring in the interior respectively at 20 km resolution. We tuned the MLI parameters to produce the same wintertime MLD as the 2 km simulation (Fig. 2**a**, black dashed curve). The Redi diffusivity was chosen as 200 $m^2\ s^{-1}$, smaller than the case above with mesoscale eddies partially resolved at 20 km resolution.

- `20 km MLI` – with the MLI parametrization at 20 km resolution.

Further details on each configuration are given in Text S4.

With appropriately tuned coefficients, the diffusive flux in 100 km GM+R run captures the amplitude and timing of cross-ML-base vertical eddy iron transport particularly around November as seen in the 2 km run (Figs. 3**b**,**e**). The vertical diffusive flux in the 100 km GM+R is the sum of KPP mixing, GM advection and Redi diffusion. Although not shown, the resolved eddy advection contribution is negligible and vertical mixing (KPP) is contained within the ML. The cross-ML-base iron transport in Fig. 3**e** is, therefore, predominantly due to isopycnal eddy stirring. Setting the Redi diffusivity to zero — equivalent to no mesoscale isopycnal stirring — in the 100-km run results in F^z_{Fe} decreasing by a factor of two. In other words, a direct comparison of vertical iron flux

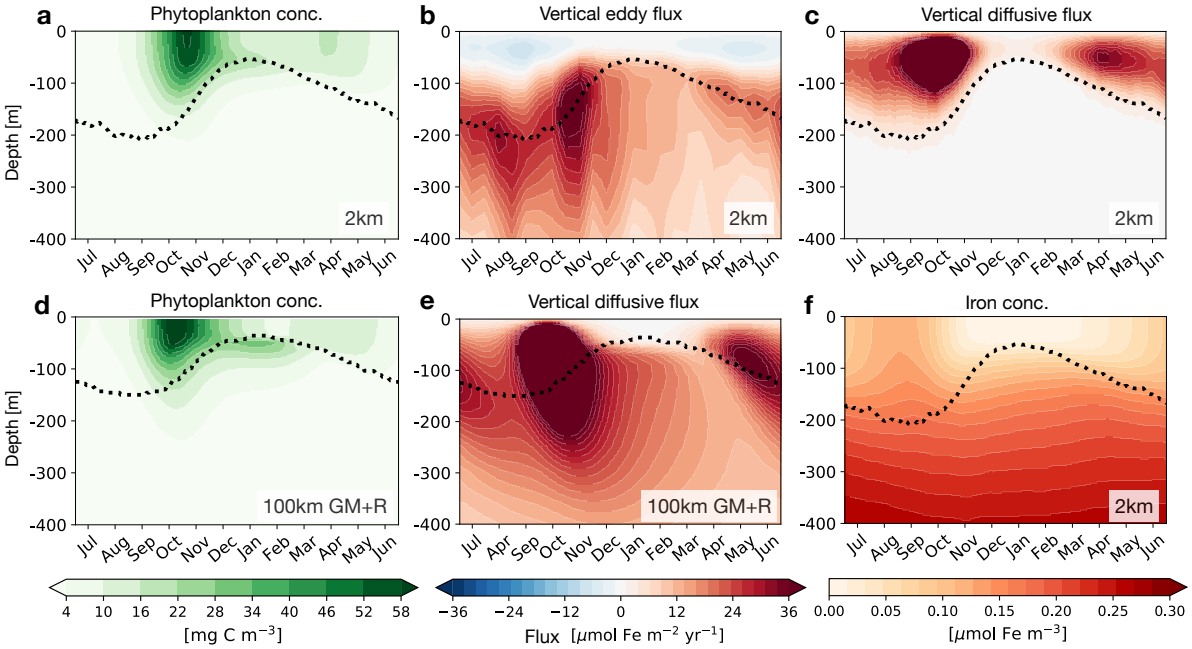

Figure 3: **Time-depth plots of the daily and spatial median of phytoplankton biomass; a. b,c** The spatial mean of vertical eddy transport using 15-daily snapshot outputs and diffusive iron transport using daily-averaged outputs. Panels **a**-**c**, and **f** (daily-averaged iron concentration) are from the 2 km run. **d,e** Daily-averaged phytoplankton biomass and vertical diffusive iron flux from the 100 km GM+R run. The dotted lines in all panels show the mixing (mixed) layer depth for the 2 km (100 km GM+R) run. The *mixing*-layer depth (MLD) was too sensitive to the winds in the 100 km GM+R run, likely due to GM interacting with KPP (39). In all of our other runs, the *mixed*-layer depth defined as the depth at which the potential temperature decreased by 0.2°C from the surface (40) (not shown), proved to be very similar to the MLD so we used the mixed-layer depth for the 100 km GM+R run.

between the 2 km and 100 km GM+R run is the sum of Fig. 3**b** and **c** against **e**. The pulse of iron coincides roughly with the spring bloom apex in early November in both cases, but summertime (January-March) biomass is lower within the top 100 m (Fig. 3**a**,**d**). The latter may be due to partially resolved MLI actively generating vertical iron gradients within the top 100 m in the 2 km run, allowing for larger diffusive flux in the top 100 m for the 2 km run than in the 100 km GM+R run (Fig. 3**c**,**e**).

We plot phytoplankton biomass against vertical iron transport also for the parametrized runs

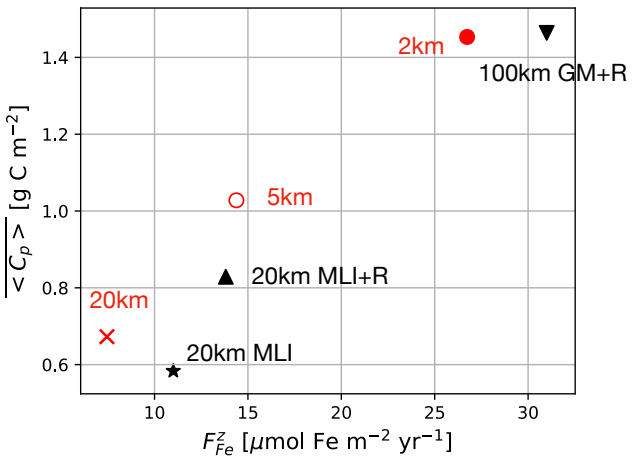

Figure 4: **The resolution dependence of annual median phytoplankton biomass ($\overline{\langle \mathbf{C_p} \rangle}$) on the annual mean of total vertical iron transport at the ML base or 100 m whichever is deeper ($F^z_{\mathbf{Fe}}$).** The runs without any eddy parametrizations are shown in red and the parametrized runs include the parametrized eddy flux.

in Fig. 4. Consistent with Fig. 3, they remain similar between the 2 km and 100 km GM+R runs (Fig. 4). The 20 km MLI+R comes close to the 5 km run (Fig. 4) with Redi diffusion adding cross-ML-base iron transport (Fig. S5). The MLI parametrization contribution, intended to replicate the restratification of the ML and not eddy tracer transport (37), is contained within the ML and does not enhance cross-ML-base iron transport (Fig. S5**b**). Isopycnals, and consequently iron contours, in the interior at 20 km resolution, however, are too steep compared to the 2 km run, with insufficient restratification relative to the resolved-mesoscale run (Figs. S4**c**, S6**b**). This results in weaker vertical gradients of iron and less net iron supply via entrainment and vertical eddy transport. The GM parametrization in the 100 km resolution run allows us to improve isopycnal steepness (Figs. S4**d**, S6**c**), and the Redi diffusivity is used to tune the isopycnal iron transport. The 20 km MLI run performs the worst amongst the parametrized runs (black markers in Fig. 4) with cross-ML-base eddy iron transport coming only from the resolved eddies at 20 km resolution.

Implications for iron budgets and biogeochemical modelling

We have shown, using a configuration representing the zonal-mean view of the Antarctic Circumpolar Current region, that eddy iron transport is crucial in supplying iron from depths across the mixing-layer base (Figs. 3, 4). Using a similar zonally-reentrant channel model, Nicholson, S. *et al*. (submitted) also found an increase in wintertime (August-October) vertical eddy iron transport, and consequently elevated primary production during September-October. Their spatial resolution of $1/24^{\circ}$, however, is similar to our 5 km run and the relative contribution of eddy transport in their study is likely underestimated (Fig. 4). Although 2 km resolution is state of the art for a basin-scale simulation coupled to a full biogeochemical model, it is not sufficient to explicitly resolve submesoscale processes including MLI (15). Based on the resolution dependence, we would expect the role of eddies in supplying iron to increase further with higher resolutions. Our results suggest that in order to adequately capture the eddy iron transport, we should either at least partially resolve the submesoscales (2km run) or completely parametrize the eddies using the current generation of GM (100km GM+R run). The agreement of the 100 km GM+R run with the 2 km run also highlights the potential significance of improving parametrization for isopycnal tracer diffusion, which has been argued to be a significant factor in tracer ventilation using shiptrack observations in the Southern and Arctic Ocean (41). In our study, the Redi diffusivity was tuned in an ad-hoc manner; future eddy parameterizations instead must be able to determine the correct value of this parameter based on physics in order to accurately simulate the response of the Southern Ocean biological pump to climate change.

Methods

Mixing layer. The mixing-layer depth (MLD) is the boundary layer over which isotropic turbulent mixing, parameterized by the KPP in this simulation, is enhanced. Here, we quantify the depth of this highly variable layer as the zonal 99$^{\text{th}}$ percentile of the daily-averaged KPP boundary layer. In our simulations, the *mixed*- and *mixing*-layer depth tended to be similar to each other. In general, however, the *mixed* layer often used in observational studies can be deeper than the *mixing* layer as the former is defined purely by thermal dynamical properties (40) while as latter is defined by kinematic properties. We argue that the *mixing* layer is the relevant depth scale for tracer transport as it is the layer over which diapycnal mixing is active (15). Figure 3**c** shows that diffusive fluxes are only active within the mixing layer in our simulation when eddies are explicitly resolved.

Integrated phytoplankton biomass. The integrated biomass ($\langle \mathrm{C_p} \rangle$) is defined as the full-depth vertical integration of the spatial median (y = 600 - 1400 km, x = 0 - 1000 km) of $\mathrm{C_p}$ in order to incorporate phytoplankon existing below the mixing layer (5). We take the median as the phytoplankton biomass in our model approximately has a log-normal distribution.

References

1. Martin, J. H., Gordon, R. M. & Fitzwater, S. E. Iron in antarctic waters. *Nature* **345**, 156 (1990).

2. De Baar, H. J. *et al.* Importance of iron for plankton blooms and carbon dioxide drawdown in the southern ocean. *Nature* **373**, 412 (1995).

3. Aumont, O. & Bopp, L. Globalizing results from ocean in situ iron fertilization studies. *Global Biogeochemical Cycles* **20** (2006).

4. Bowie, A. R. *et al.* Biogeochemical iron budgets of the southern ocean south of australia: Decoupling of iron and nutrient cycles in the subantarctic zone by the summertime supply. *Global Biogeochemical Cycles* **23** (2009).

5. Llort, J., Lévy, M., Sallée, J.-B. & Tagliabue, A. Onset, intensification, and decline of phytoplankton blooms in the southern ocean. *ICES Journal of Marine Science: Journal du Conseil* **72**, 1971–1984 (2015).

6. Tagliabue, A. *et al.* Surface-water iron supplies in the southern ocean sustained by deep winter mixing. *Nature Geoscience* **7**, 314–320 (2014).

7. Moore, J. K., Lindsay, K., Doney, S. C., Long, M. C. & Misumi, K. Marine ecosystem dynamics and biogeochemical cycling in the community earth system model [cesm1 (bgc)]: Comparison of the 1990s with the 2090s under the rcp4. 5 and rcp8. 5 scenarios. *Journal of Climate* **26**, 9291–9312 (2013).

8. Moore, C. *et al.* Processes and patterns of oceanic nutrient limitation. *Nature geoscience* **6**, 701–710 (2013).

9. Verdy, A. & Mazloff, M. A data assimilating model for estimating southern ocean biogeochemistry. *Journal of Geophysical Research: Oceans* **122**, 6968–6988 (2017).

10. Tagliabue, A. *et al.* How well do global ocean biogeochemistry models simulate dissolved iron distributions? *Global Biogeochemical Cycles* **30**, 149–174 (2016).

11. Gnanadesikan, A., Pradal, M.-A. & Abernathey, R. Isopycnal mixing by mesoscale eddies significantly impacts oceanic anthropogenic carbon uptake. *Geophysical Research Letters* **42**, 4249–4255 (2015).

12. Wolfe, C., Cessi, P., McClean, J. & Maltrud, M. Vertical heat transport in eddying ocean models. *Geophysical Research Letters* **35** (2008).

13. Griffies, S. M. *et al.* Impacts on ocean heat from transient mesoscale eddies in a hierarchy of climate models. *Journal of Climate* **28**, 952–977 (2015).

14. Zika, J. D. *et al.* Vertical eddy fluxes in the southern ocean. *Journal of Physical Oceanography* **43**, 941–955 (2013).

15. Balwada, D., Smith, K. S. & Abernathey, R. Submesoscale vertical velocities enhance tracer subduction in an idealized antarctic circumpolar current. *Geophysical Research Letters* **45**, 9790–9802 (2018).

16. McWilliams, J. C. Submesoscale currents in the ocean. *Proc. R. Soc. A* **472**, 20160117 (2016).

17. Lévy, M., Ferrari, R., Franks, P. J., Martin, A. P. & Rivière, P. Bringing physics to life at the submesoscale. *Geophysical Research Letters* **39** (2012).

18. Rosso, I. *et al.* Vertical transport in the ocean due to sub-mesoscale structures: Impacts in the kerguelen region. *Ocean Modelling* **80**, 10–23 (2014).

19. Rosso, I., Hogg, A. M., Matear, R. & Strutton, P. G. Quantifying the influence of sub-

277 mesoscale dynamics on the supply of iron to southern ocean phytoplankton blooms. *Deep*
278 *Sea Research Part I: Oceanographic Research Papers* **115**, 199–209 (2016).

279 20. Abernathey, R., Ferreira, D. & Klocker, A. Diagnostics of isopycnal mixing in a circumpolar
280 channel. *Ocean Modelling* **72**, 1–16 (2013).

281 21. Abernathey, R. & Ferreira, D. Southern ocean isopycnal mixing and ventilation changes driven
282 by winds. *Geophysical Research Letters* **42**, 10–357 (2015).

283 22. Marshall, J., Adcroft, A., Hill, C., Perelman, L. & Heisey, C. A finite-volume, incompressible
284 navier stokes model for studies of the ocean on parallel computers. *Journal of Geophysical*
285 *Research: Oceans* **102**, 5753–5766 (1997).

286 23. Dutkiewicz, S., Follows, M. J. & Bragg, J. G. Modeling the coupling of ocean ecology and
287 biogeochemistry. *Global Biogeochemical Cycles* **23** (2009).

288 24. Gloege, L., McKinley, G. A., Mouw, C. B. & Ciochetto, A. B. Global evaluation of partic-
289 ulate organic carbon flux parameterizations and implications for atmospheric pco2. *Global*
290 *Biogeochemical Cycles* **31**, 1192–1215 (2017).

291 25. Lévy, M., Franks, P. J. & Smith, K. S. The role of submesoscale currents in structuring marine
292 ecosystems. *Nature communications* **9**, 4758 (2018).

293 26. Boyd, P. W. & Ellwood, M. J. The biogeochemical cycle of iron in the ocean. *Nature Geo-*
294 *science* **3**, 675–682 (2010).

295 27. Orsi, A. H., Whitworth III, T. & Nowlin Jr, W. D. On the meridional extent and fronts of the

antarctic circumpolar current. *Deep Sea Research Part I: Oceanographic Research Papers* **42**, 641–673 (1995).

28. Sallée, J.-B., Llort, J., Tagliabue, A. & Lévy, M. Characterization of distinct bloom phenology regimes in the southern ocean. *ICES Journal of Marine Science: Journal du Conseil* **72**, 1985–1998 (2015).

29. Ardyna, M. *et al.* Delineating environmental control of phytoplankton biomass and phenology in the southern ocean. *Geophysical Research Letters* **44**, 5016–5024 (2017).

30. Boccaletti, G., Ferrari, R. & Fox-Kemper, B. Mixed layer instabilities and restratification. *Journal of Physical Oceanography* **37**, 2228–2250 (2007).

31. Behrenfeld, M. J. & Boss, E. S. Student's tutorial on bloom hypotheses in the context of phytoplankton annual cycles. *Global change biology* **24**, 55–77 (2018).

32. Large, W. G., McWilliams, J. C. & Doney, S. C. Oceanic vertical mixing: A review and a model with a nonlocal boundary layer parameterization. *Reviews of Geophysics* **32**, 363–403 (1994).

33. Hallberg, R. Using a resolution function to regulate parameterizations of oceanic mesoscale eddy effects. *Ocean Modelling* **72**, 92–103 (2013).

34. Gent, P. R. & Mcwilliams, J. C. Isopycnal mixing in ocean circulation models. *Journal of Physical Oceanography* **20**, 150–155 (1990).

35. McDougall, T. J. & McIntosh, P. C. The temporal-residual-mean velocity. part ii: Isopycnal

interpretation and the tracer and momentum equations. *Journal of Physical Oceanography* **31**, 1222–1246 (2001).

36. Redi, M. H. Oceanic isopycnal mixing by coordinate rotation. *Journal of Physical Oceanography* **12**, 1154–1158 (1982).

37. Fox-Kemper, B. *et al.* Parameterization of mixed layer eddies. iii: Implementation and impact in global ocean climate simulations. *Ocean Modelling* **39**, 61–78 (2011).

38. Visbeck, M., Marshall, J., Haine, T. & Spall, M. Specification of eddy transfer coefficients in coarse-resolution ocean circulation models. *Journal of Physical Oceanography* **27**, 381–402 (1997).

39. Ferrari, R., McWilliams, J. C., Canuto, V. M. & Dubovikov, M. Parameterization of eddy fluxes near oceanic boundaries. *Journal of Climate* **21**, 2770–2789 (2008).

40. de Boyer Montégut, C., Madec, G., Fischer, A. S., Lazar, A. & Iudicone, D. Mixed layer depth over the global ocean: An examination of profile data and a profile-based climatology. *Journal of Geophysical Research: Oceans* **109** (2004).

41. Naveira Garabato, A. C. *et al.* High-latitude ocean ventilation and its role in earth's climate transitions. *Philosophical Transactions of the Royal Society A: Mathematical, Physical and Engineering Sciences* **375**, 20160324 (2017).

Acknowledgements This research was supported by NASA Award NNX16AJ35G as part of the SWOT Science Team. Abernathey acknowledges additional support from NSF Award OCE-1553593.

Additional information Supplementary information is available in the online version of the paper. The model configuration is available on Github (doi:10.5281/zenodo.3266400) and simulation outputs for 15-daily snapshot and monthly-averaged outputs of physical variables ($\mathbf{v}, \theta, \Phi$) are available on Pangeo (doi:10.5281/zenodo.3358021). Correspondence and requests for other variables and materials should be addressed to the leading author (email: takaya@ldeo.columbia.edu)

Competing Interests The authors declare that they have no competing financial interests.